Remote Sensing of Environment xxx (2015) xxx–xxx

Contents lists available at ScienceDirect

Remote Sensing of Environment

journal homepage: www.elsevier.com/locate/rse

Improved surface temperature estimates with MASTER/AVIRIS sensor fusion

Shane P. Grigsby [a,b,*], Glynn C. Hulley [c], Dar A. Roberts [b], Christopher Scheele [d], Susan L. Ustin [e], Maria Mar Alsina [e]

[a] Cooperative Institute for Research in Environmental Sciences, University of Colorado, Boulder, CO 80309, United States
[b] Department of Geography, University of California Santa Barbara, CA 93106, United States
[c] Jet Propulsion Laboratory, California Institute of Technology, Pasadena, CA 91109, United States
[d] Atmospheric and Oceanic Sciences, University of Wisconsin-Madison, WI 53706, United States
[e] Dept. of Land, Air and Water Resources, University of California Davis, CA 95616, United States

ARTICLE INFO

Article history:
Received 16 June 2014
Received in revised form 14 May 2015
Accepted 20 May 2015
Available online xxxx

Keywords:
Canopy temperature
Validation
Water vapor scaling
Land surface temperature
HyspIRI
Thermal infrared
MASTER

ABSTRACT

Land surface temperature (LST) is an important parameter in many ecological studies. The current Root Mean Square Error (RMSE) in standard MODIS and ASTER LST products is greater than 1 K, and for ASTER can be as large as 4 K for graybody pixels such as vegetation. Errors of 3 to 8 K have been observed for ASTER in humid conditions, making knowledge of atmospheric water vapor content critical in retrieving accurate LST. For this reason improved accuracy in LST measurements through the synthesis of visible-to-shortwave-infrared (VSWIR) derived water vapor maps and Thermal-Infrared (TIR) data is one goal of the Hyperspectral Infrared Imager, or HyspIRI, mission. The 2011 ER-2 Delano/Lost Hills flights acquired data with both the MODIS/ASTER Simulator (MASTER) and Airborne Visible InfraRed Imaging Spectrometer (AVIRIS) instruments flown concurrently. This study compares LST retrieval accuracies from the standard JPL MASTER temperature products produced using the temperature–emissivity separation (TES) algorithm, and the water vapor scaling (WVS) atmospheric correction method proposed for HyspIRI. The two retrieval methods are run both with and without high spatial resolution AVIRIS-derived water vapor maps to assess the improvement from VSWIR synthesis. We find improvement using VSWIR derived water vapor maps, with the WVS method being most accurate overall. For closed canopy agricultural vegetation we observed temperature retrieval RMSEs of 0.49 K and 0.70 K using the WVS method on MASTER data with and without AVIRIS derived water vapor, respectively.

1. Introduction

Kinetic temperature exerts a measurable effect on most physical processes, and is explicitly used as an input to model both plant water stress (Jackson, Idso, Reginato, & Pinter, 1981) and evapotranspiration (Allen, Pereira, Raes, & Smith, 1998; Monteith et al., 1965). Water stress and evapotranspiration are of particular interest to farmers in semiarid drought prone regions such as California, where agricultural production was valued at $44.7 billion in 2012 (CDFA, 2013). A 32.5% water delivery reduction was predicted in the California Central Valley as a result of 2014 drought, which had an estimated total economic loss of $1.67 billion (Howitt, Medellin-Azuara, & Lund, 2014). The socioeconomic effects of the current drought are predicted to be 50% more severe than those resulting from the 2009 drought. Reduced access to water may result in higher cost for water, reduced yields from existing fields, and abandonment (Howitt et al., 2014). Accurate modeling of temperature and evapotranspiration provides farmers with robust estimates of water demand, enabling more conservative and efficient agricultural water use that reduces the agricultural impact of drought.

Plant water stress in general limits photosynthetic activity, decreasing growth and compromising yield (Kliewer, Freeman, & Hossom, 1983; Schultz & Matthews, 1988). For woody perennial crops—a group that includes the two largest irrigated crops in California, vineyards ($4.45 billion, 2012) and almond orchards ($4.35 billion, 2012) (CDFA, 2013)—seasonal management of plant water stress is particularly crucial for achieving the maximum yield with the desired quality. In grapevines, for example, the process from cluster differentiation to full maturation covers two seasons, resulting in a yield loss due to water stress that extends beyond a single season (Matthews & Anderson, 1989), and, in extreme cases, a requirement for redrafting or replanting.

The ability of vines to adapt to plant available soil water varies by grape variety or rootstock-variety combinations. The term *plant water status* refers not only to the plant water content but how water content impacts plant functioning. For correct irrigation scheduling that seasonally modulates water status as desired, the crop evapotranspiration and the plant water status need to be monitored in parallel.

* Corresponding author at: Cooperative Institute for Research in Environmental Sciences, University of Colorado, Boulder, CO 80309, United States.
E-mail address: shane@geog.ucsb.edu (S.P. Grigsby).

http://dx.doi.org/10.1016/j.rse.2015.05.019
0034-4257/

Leaf and stem water potential are accepted as good indicators of plant water status in orchards and vineyards (Escalona, Flexas, & Medrano, 2000; Flexas et al., 2004; McCutchan & Shackel, 1992) and both parameters show good correlation with stomatal conductance—which is itself the foremost mechanism of response to water stress in plants (Hsiao, 1973). Plant water demand and status change spatially with variability within an orchard or vineyard, but irrigation is often scheduled based on discrete measurements of plant water status at a few sites in the orchard or vineyard, mainly leaf or stem water potential (Girona et al., 2006; Shackel et al., 1997). These irrigation decisions can result in substantial over irrigation of certain areas, and/or plant status compromise in others. While discrete *in situ* measurements are valuable tools for farmers, the size and scope of agriculture—10.28 million hectares and 80,500 farms in 2012 for California alone (CDFA, 2013)—underscore the necessity for accurate regional scale remote sensing measurements that can be used to assess evapotranspiration, water status, and other parameters that support decision making for agricultural practices.

The accuracy of remote sensing temperature measurements is of particular importance in assessing water stress and evapotranspiration (Anderson et al., 2008). Since leaf stomatal closure results in an increase of leaf temperature, the temperature gradient (dT) between leaf surface and the surrounding air serves as a good indicator of vine water stress. The temperature gradient between the air and leaves can be less than 1 K for vegetation in semiarid ecosystems (Jarvis & McNaughton, 1986), however, current remotely sensed Land Surface Temperature (LST) estimates typically have errors on the order of 1 K when averaged over rocks, soils, sands and graybodies (Hulley, Hughes, & Hook, 2012). While the main driver of evapotranspiration is the vapor pressure gradient between the leaves and the atmosphere, the saturation vapor pressure which determines the gradient is itself temperature dependent, and accurate temperature estimates are needed as input to evapotranspiration models (Courault, Seguin, & Olioso, 2005). Errors up to 4 K are typical for spectral graybodies such as vegetation (Gustafson, Gillespie, & Yamada, 2006), due to uncertainty in emissivity and errors in atmospheric correction from elevated moisture over large contiguous vegetation patches. Even for targets with well known emissivity such as water surfaces, errors as large as 3–8 K can occur under humid conditions (Tonooka, 2005), and robust atmospheric correction of thermal data is still essential in less humid Mediterranean climates to provide accurate estimates of LST.

The development of smaller high quality multiband thermal imagers and hyperspectral sensors has made it possible to acquire high spatial resolution thermal and hyperspectral data in tandem from an aircraft or a satellite. In this paper we evaluate two current thermal infrared (TIR) temperature retrieval algorithms, and compare the temperature retrievals with *in situ* measurements of leaf temperature. In particular, we investigate leveraging hyperspectral data to estimate per-pixel atmospheric water vapor and improve the atmospheric correction of paired thermal data. More specifically, we paired Airborne Visible-InfraRed Imaging Spectrometer (AVIRIS) and MODIS–ASTER Simulator (MASTER) data to quantify potential improvements in temperature retrieval accuracy for both the temperature–emissivity separation (TES) algorithm and the water vapor scaling (WVS) method.

1.1. Theoretical background

Atmospheric correction of thermal data can be accomplished by a number of methods, however all methods focus on solving the same physical equation:

$$L_\lambda = \left[\epsilon_\lambda B_\lambda(T_s) + (1-\epsilon_\lambda) * L_\lambda^{\downarrow}\right] * \tau_\lambda + L_\lambda^{\uparrow} \quad (1)$$

where L_λ is the at-sensor thermal radiance; ϵ_λ is an unknown emissivity; $B_\lambda(T_s)$ is the blackbody radiance at surface temperature T_s as given by the Planck function $B_\lambda()$; $L_\lambda^{\downarrow}$ and $L_\lambda^{\uparrow}$ are the downwelling and upwelling long wave radiance from the atmosphere; and τ_λ is the transmittance from the ground to the sensor. The surface temperature T_s is the only term that does not vary spectrally; the at-sensor radiance L_λ is the data acquired by MASTER. The $L_\lambda^{\downarrow}$ and $L_\lambda^{\uparrow}$ terms are atmospheric emittance terms that vary per pixel, and are determined by atmospheric composition and state, as is per pixel transmittance to the sensor.

Estimating LST from remotely sensed data is challenging in part because the emissivity of a surface, which varies spectrally, is required to invert the Planck function and retrieve LST (Zhengming & Dozier, 1989). Solving for emissivity and LST simultaneously results in an underdetermined system of equations, with n observations being used to solve for both a single temperature, and n emissivities (Realmuto, 1990). Errors in emissivity estimation directly affect temperature retrieval accuracy during the Planck inversion and additional errors are added when correcting for downwelling atmospheric radiance that is reflected off of the land surface. Current techniques such as the TES algorithm (Gillespie et al., 1998), have sought to constrain the emissivity solution space through the use of empirically established relationships related to the Minimum–Maximum Difference (MMD) in emissivity (Matsunaga, 1994), or other related measures of contrast in the emissivity spectrum. Unfortunately, these techniques are not effective over graybody pixels with low ϵ_λ spectral contrast, such as vegetation, in part due to residual effects of incomplete atmospheric correction. The WVS technique attempts to minimize the effects of both these atmospheric residuals and sensor noise by using an estimate of water vapor and sensor simulation data to scale the $L_\lambda^{\downarrow}$, $L_\lambda^{\uparrow}$ and τ_λ terms.

While well mixed atmospheric gasses such as CO_2 and O_3 can be estimated and corrected using regional estimates or model data from the National Center for Environmental Prediction (NCEP), significant challenges remain in correcting thermal imagery to account for column water vapor, an atmospheric constituent that varies temporally and spatially and is not well mixed (Gao & Goetz, 1990). One solution to account for this variability is to invert for column water vapor by comparing measured radiance to modeled radiance using radiative transfer code such as MODTRAN (Berk, Bernstein, & Robertson, 1987; Berk et al., 1998, 2005) while allowing water vapor to vary on a per-pixel basis (Green, Conel, & Roberts, 1993). Direct physical inversion for water vapor in the Thermal-InfraRed (TIR) portion of the spectrum is complicated both by the multisource nature of TIR emissions, and by low signal to noise ratios within the TIR; hence broadband sensors that include TIR channels such as the MODerate Resolution Imaging Spectrometer (MODIS) typically utilize the higher signal to noise ratios and single source nature of the Visible Short Wave InfraRed (VSWIR) channels to solve for total column water vapor. Since water absorption features within spectra are defined by their depth, width, and shape (Carrère & Conel, 1993), high spectral resolution sensors such as the hyperspectral Airborne Visible/InfraRed Imaging Spectrometer (AVIRIS) are better able to retrieve total column water vapor relative to broadband sensors such as the MODIS–ASTER Simulator (MASTER), which appears to underestimate total column water vapor (Roberts, Quattrochi, Hulley, Hook, & Green, 2012; Scheele, Rill, Grigsby, & Ustin, 2013). Given that uncertainty of column water vapor dominates as a source of atmospheric error when retrieving temperature from remotely sensed imagery (Hook, Myers, Thome, Fitzgerald, & Kahle, 2001), the fusion of broadband thermal imagery with shortwave hyperspectral imagery opens synergistic opportunities for improving temperature retrievals (Roberts et al., 2012).

1.2. Science objectives and relevance to HyspIRI

The National Research Council has recommended the HyspIRI mission. HyspIRI combines a 213-channel VSWIR imaging spectrometer with an 8-channel TIR radiometer, and would enable global simultaneous acquisition and synergy of hyperspectral VSWIR and TIR data at spatial resolutions comparable to Landsat (Roberts et al., 2012). In this paper, we assess the capabilities of HyspIRI-like instrumentation in

Please cite this article as: Grigsby, S.P., et al., Improved surface temperature estimates with MASTER/AVIRIS sensor fusion, *Remote Sensing of Environment* (2015), http://dx.doi.org/10.1016/j.rse.2015.05.019

retrieving vegetation canopy temperature by comparing *in situ* leaf temperature measurements with temperatures retrieved using only TIR MASTER data, and temperatures retrieved using a synthesis of MASTER and AVIRIS remote sensing data. Specifically, we compare temperature estimates from the following five methods of temperature retrieval with *in situ* field data:

1. Single band inversion using AVIRIS derived water vapor to estimate per pixel $L_\lambda^\downarrow$, $L_\lambda^\uparrow$ and τ_λ.
2. TES with $L_\lambda^\downarrow$, $L_\lambda^\uparrow$ and τ_λ terms derived from user supplied atmospheric terms, including a scene estimate of water vapor.
3. TES with per pixel $L_\lambda^\downarrow$, $L_\lambda^\uparrow$ and τ_λ terms supplied from AVIRIS derived water vapor, as in the single band case.
4. WVS method applied with NCEP estimates of water vapor used to scale $L_\lambda^\downarrow$, $L_\lambda^\uparrow$ and τ_λ terms derived from NCEP atmospheric profiles.
5. WVS applied using AVIRIS derived per pixel water vapor to scale $L_\lambda^\downarrow$, $L_\lambda^\uparrow$ and τ_λ terms generated from NCEP atmospheric profiles.

The WVS method was selected due to the increased accuracy that it offers in humid conditions where large uncertainties usually exist from remote sensing or model derived water vapor profiles (Hulley, Veraverbeke, & Hook, 2014; Tonooka, 2005), and also because it is the candidate algorithm for temperature retrievals for the future HyspIRI mission. TES was selected since it is the current temperature retrieval algorithm in use for ASTER and MODIS; the MASTER-TES algorithm runs as a submodule to the WVS method, and comparison between the two showcases expected improvements between the two methods. Single band inversion is the closest approximation to an unmodified application of Eq. (1), and is used as a control between improvements in emissivity retrieval versus improvements in atmospheric correction. The differences in the Fields Of View (FOVs) in the broadband TIR radiometer and SWIR spectrometer on HyspIRI will result in significant portions of the larger TIR swath that are not imaged by the VSWIR spectrometer; comparison of methods using NCEP and per pixel water vapor allows quantification of gains in temperature retrieval accuracy that can be expected within the overlapping scan area.

These comparisons allow us to quantify the improvement that hyperspectral data bring to TIR temperature retrievals. They also provide insight into the magnitude and potential sources of remaining uncertainty in temperature retrievals. We validate and assess LST retrieval accuracy using *in situ* measurements. Accuracy assessment of temperature retrievals is important to know what physical processes we are able to model, as well as what new phenomena we will be able to explore using HyspIRI-like sensors.

2. Materials and methods

2.1. Study area

Our study is focused on a 15 hectare (ha) production agriculture site in the San Joaquin Valley owned by Delano Vineyards. The vineyard produces Crimson seedless table grapes, and was split into two 7.5 ha blocks (North and South) that received two different watering regimes as part of a research study investigating the detection of vine water status using remote sensing (Alsina et al., 2013). Starting on April 8th 2011, and continuing throughout the growing season, the North block was fully irrigated to cover vine water demand while the South block had irrigation completely stopped 10 days prior to data collection, which produced a range of canopy temperatures and plant water physiologic status. The availability of remote sensing data over this site, combined with the range of vegetation conditions, closed canopies, and presence of both *in situ* instrumentation and sampling were the primary factors that led us to select Delano Vineyards for this study.

2.2. Remote sensing data

As part of a larger experiment investigating canopy water content (Cheng, Riaño, & Ustin, 2014; Cheng et al., 2013), a number of flight lines over almond orchards and vineyards were flown throughout the San Joaquin Valley in 2011 with the MASTER and AVIRIS remote sensing instruments. While these flights included morning and afternoon flights over Delano Vineyards, we selected only the Delano afternoon flight for our remote sensing analysis because the data were acquired closer in time to our *in situ* sampling data. The NASA ER2 passed over our field site at Delano Vineyards at 15:01 local time (PST; 22:01 UTC) on May 20th 2011 at an altitude of 8.3 km carrying both the AVIRIS and MASTER instruments. The orthorectified and overlaid images in Fig. 2 show the result of both the different sensor swath widths (FOVs) and spatial resolutions (IFOVs). The flight speed resulted in an oversampled area of interest, leading to higher effective spatial resolutions compared to the instrument IFOVs—6.9 m for AVIRIS and 13.1 m for MASTER. We found the MASTER georeferenced product to be highly spatially accurate over our field site, with the corners of the north and south data blocks in the MASTER imagery aligned to ground sampled GPS points

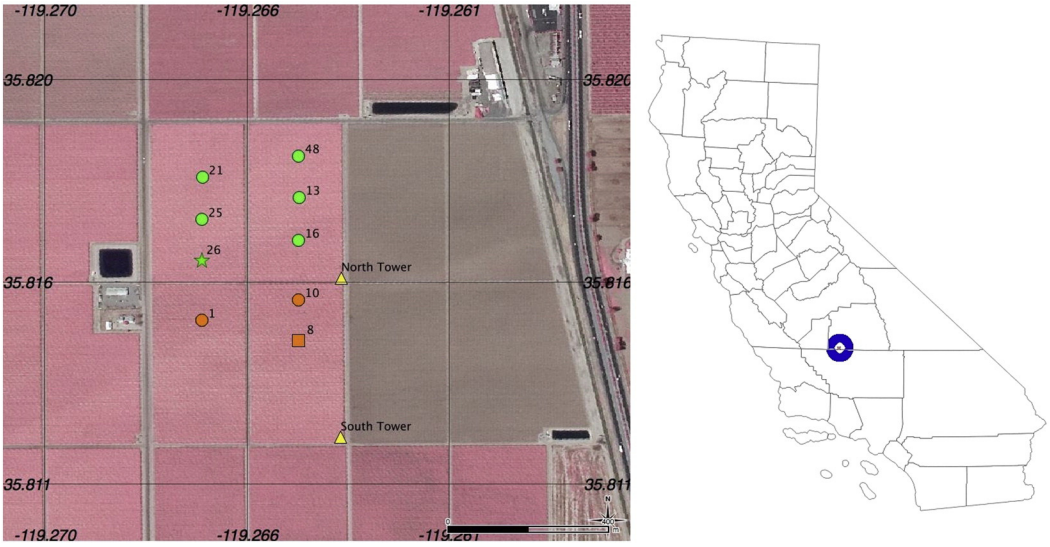

Fig. 1. Field site at Delano Vineyards. Yellow triangles show locations of towers; numbered glyphs indicate data vines that were sampled. Vine 26 ('★') was sampled only during predawn; vine 8 ('■') was sampled only during the afternoon; all other data vines were sampled at both times. Vine glyphs are colored green for north block samples and orange for south block samples. The highway at the right of the image is California State Route 99 (SR 99).

Please cite this article as: Grigsby, S.P., et al., Improved surface temperature estimates with MASTER/AVIRIS sensor fusion, *Remote Sensing of Environment* (2015), http://dx.doi.org/10.1016/j.rse.2015.05.019

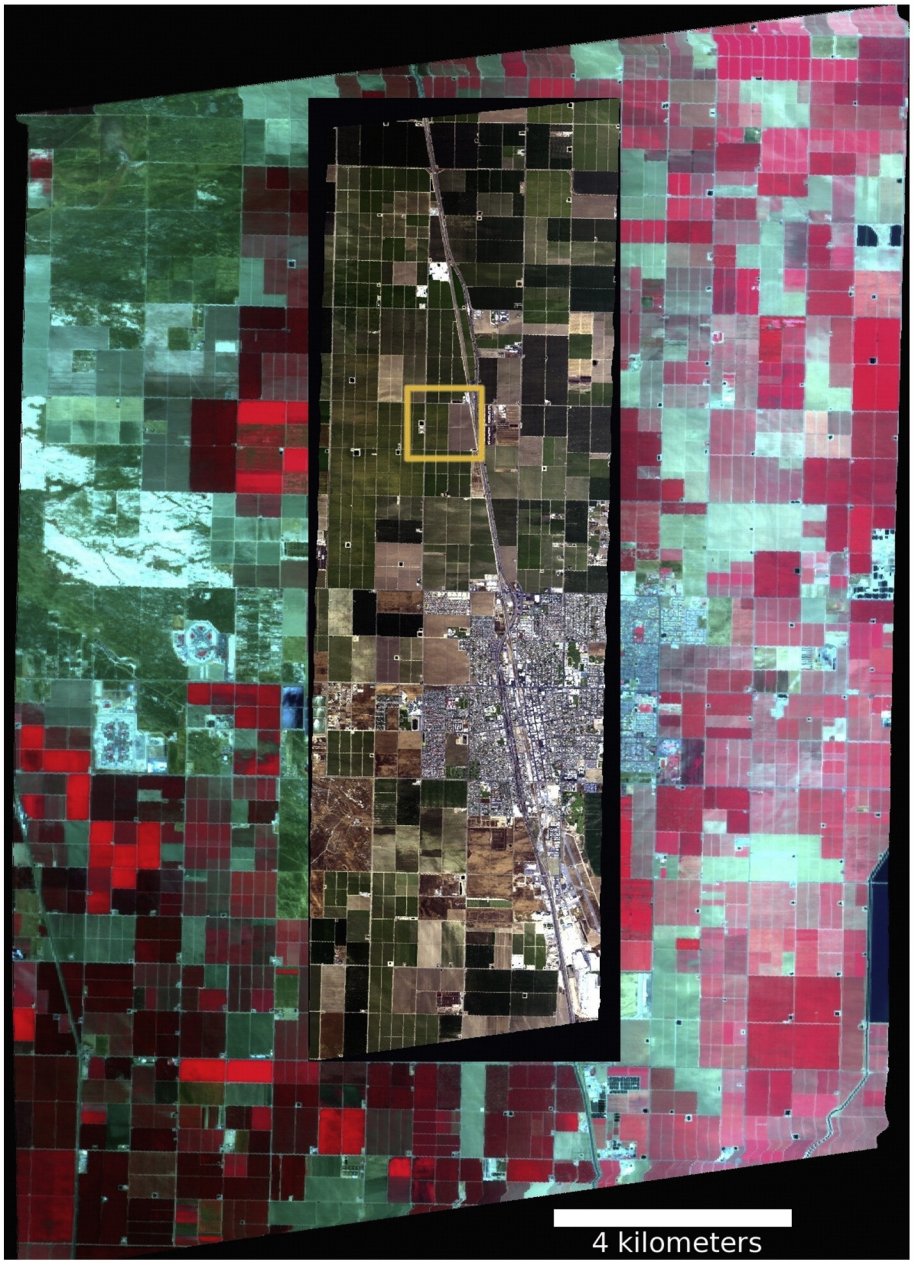

Fig. 2. MASTER and AVIRIS flight lines; yellow box is the field site shown in Fig. 1. MASTER bands: Red = 9, green = 5, blue = 3; AVIRIS bands: red = 29, green = 20, blue = 11.

with subpixel accuracy and not in need of further spatial correction or georegistration.

2.2.1. AVIRIS water vapor retrieval

We retrieved precipitable column water vapor for the AVIRIS flight line using the ACORN atmospheric correction software run in mode 1.5 with a tropical atmosphere profile. The tropical atmosphere profile was used in ACORN because the starting surface temperature of this profile more closely matched the surface temperature of the *in situ* data, and the atmospheric conditions of the heavily irrigated Central Valley in May are better approximated by the tropical profile in MODTRAN than by the mid-latitude summer profile. Additionally, the mid-latitude summer profile was prone to saturate water vapor estimates over moist pixels due to the lower saturation vapor pressure that this cooler temperature profile provides. Liquid water within the canopy was also simultaneously retrieved in ACORN to avoid overestimation of water vapor from mixing of the adjacent liquid and vapor water absorption features (Gao & Goetz, 1990). Both the 940 nm and 1140 nm water absorption features were used for the inversion, with aerosol path scattered radiance included within the fit. ACORN optimized visibility, the parameter that accounts for aerosols within ACORN, to a value of 20 km from an initial estimate of 16 km provided from the nearest airport in Bakersfield, CA.

Despite the higher spatial resolution of AVIRIS, higher accuracy georegistration within the MASTER data product led us to use MASTER as the authoritative basemap when coregistering the MASTER and AVIRIS datasets. To register the datasets we first resized the 6.9 m pixels of the AVIRIS imagery and AVIRIS derived water vapor map to match the larger 13.1 m MASTER pixels using pixel aggregate resampling. The resampled visible bands of AVIRIS were registered to the visible bands of MASTER applying pixel offsets to translate the AVIRIS image and align linear features present in the imagery. Specifically, the resampled AVIRIS data were shifted 2 pixels east and one pixel north in order to match the corners of the data blocks and align the roads. These same pixel offsets found in the visible AVIRIS imagery were used to translate and register the AVIRIS derived water vapor map.

Please cite this article as: Grigsby, S.P., et al., Improved surface temperature estimates with MASTER/AVIRIS sensor fusion, *Remote Sensing of Environment* (2015), http://dx.doi.org/10.1016/j.rse.2015.05.019

2.2.2. Thermal infrared data preprocessing

We selected five MASTER bands from the TIR for thermal temperature retrieval processing: bands 43 (8.62 μm), 44 (9.09 μm), 47 (10.64 μm), 48 (11.33 μm), and 49 (12.12 μm). These bands were selected to best approximate the HyspIRI proposed bands centered at 8.63 μm, 9.07 μm, 10.53 μm, 11.33 μm, and 12.05 μm. Although MASTER band 42 (8.18 μm) approximates the proposed 8.28 μm HyspIRI band, we excluded this band in our processing due to potential methane contamination, an atmospheric component that was not explicitly modeled in this study. Additionally, MASTER band 41 (7.81 μm) was also excluded as it has little overlap with the HyspIRI band at 7.35 μm. The MASTER instrument's Spectral Response Functions (SRFs), which were used to convolve MODTRAN modeled atmospheric path radiance terms, were derived from empirical monochromator measurements made prior to the data flights at NASA Ames on May 11th, 2011. Radiometrically corrected MASTER L1B data was used for at sensor radiance.

2.2.3. Single band inversion

Temperature retrieval from thermal data consists of three broad steps: 1) atmospheric correction of at sensor radiance to at ground emitted radiance; 2) estimation of target emissivity; and 3) inversion to physical temperature using estimated target emission and emissivity. The single band inversion method follows an initial correction routine similar to TES and WVS, but separates atmospheric correction error from TES emissivity estimation error by bypassing the TES module and prescribing an *a priori* fixed value of the maximum spectral surface emissivity for one band. The maximum spectral graybody emissivity of vegetation ranges from 0.97 to 0.99, and since our pixels are smaller and less heterogeneous than either MODIS or ASTER, we set a value of 0.99 for maximum spectral emissivity in the initial atmospheric correction.

To correct sensor radiance to emitted ground radiance, we ran MODTRAN to generate 42 different atmospheric models, varying precipitable water vapor from 1.00 to 1.82 g/cm^2 in 0.02 g/cm^2 increments. The input parameters for MODTRAN runs were taken from the AVIRIS atmospheric correction detailed in Section 2.2.1, with additional atmospheric constituents estimated from NCEP as appropriate. Each MODTRAN run yielded water vapor dependent values of $L_\lambda^\uparrow$, $L_\lambda^\downarrow$, and τ_λ from 8 μm to 14 μm at a spectral resolution of 1 cm^{-1}, which were then convolved to the MASTER bands using the May 11th SRFs provided by NASA Ames. We fit univariate splines between the different water vapor model runs to create forward Look Up Tables (LUTs) in the thermal region, an approach that is a modification of Green, Conel, Margolis, Bruegge, and Hoover's (1991) method to generate reverse LUTs for atmospheric correction. Our LUTs thus mapped any given amount of precipitable water vapor between 1.00 to 1.82 g/cm^2 to interpolated MODTRAN $L_\lambda^\uparrow$, $L_\lambda^\downarrow$, and τ_λ terms convolved to the MASTER instrument.

We processed the MASTER TIR data using the following equation:

$$\left[\left(L_\lambda - L_\lambda^\uparrow\right)/\tau_\lambda\right] - (0.01) * L_\lambda^\downarrow = 0.99 * B_\lambda(T_s) \tag{2}$$

where Eq. (2) is identical to Eq. (1), but assumes an initial value of $\epsilon_\lambda = 0.99$ for all bands. The $L_\lambda^\uparrow$, $L_\lambda^\downarrow$, and τ_λ values per pixel were estimated by looking up column water vapor from the corresponding AVIRIS water vapor pixel described in Section 2.2.1, and retrieving the corresponding $L_\lambda^\uparrow$, $L_\lambda^\downarrow$, and τ_λ values from the thermal LUTs. Taking the per pixel hottest band as the closest to true surface temperature, we calculated the relative emissivity for the other bands assuming a physical temperature equal to the hottest band. The final per band temperatures were estimated by using the same $L_\lambda^\uparrow$, $L_\lambda^\downarrow$, and τ_λ values per pixel applied to Eq. (1) with the calculated relative emissivities applied to reduce error in the reflected $L_\lambda^\downarrow$ component; the average of the Planck inversion temperatures for all five bands yielded the retrieved temperature.

2.2.4. Temperature and emissivity separation (TES)

The TES algorithm (Gillespie et al., 1998; Gustafson et al., 2006) uses the procedure described in Section 2.2.3. To solve for the emissivity, an empirical relationship is used that correlates spectral contrast between a specific set of bands and the minimum emissivity, ϵ_{min}, of laboratory measured surface types as described in Baldridge, Hook, Grove, and Rivera (2009) and Hulley and Hook (2009). The regression for MASTER bands 43, 44, 47, 48, and 49 is shown in Fig. 3, as well as in Eq. (3) below:

$$\epsilon_{min} = 0.9921 - 0.74329 * MMD^{0.78522} \tag{3}$$

where $MMD = Max(\epsilon_\lambda^{stand}) - Min(\epsilon_\lambda^{stand})$.

Following an initial atmospheric correction with Eq. (2), we calculated the standardized emissivity (ϵ_λ^{stand}) by dividing the per pixel relative emissivities from Section 2.2.3 by the pixel mean of those relative emissivities. We calculated the MMD and ϵ_{min} per pixel using Eq. (3), and then used Eq. (4) to solve for calibrated emissivity (ϵ_λ^{cal}):

$$\epsilon_\lambda^{cal} = \epsilon_\lambda^{stand} * \left[\epsilon_{min} / min\left(\epsilon_\lambda^{stand}\right)\right] \tag{4}$$

where $min(\epsilon_\lambda^{stand})$ is the minimum standardized emissivity for a pixel among all of the bands used for the correction. The ϵ_λ^{cal} was then used with Eq. (1), and as in Section 2.2.3, the average temperature from MASTER bands 43, 44, 47, 48, and 49 was considered the retrieved temperature. In addition to using the per pixel estimates of $L_\lambda^\uparrow$, $L_\lambda^\downarrow$, and τ_λ provided from the AVIRIS water vapor map, this procedure was applied to generate the JPL standard product. The JPL standard product is available for all MASTER flight lines and uses scene estimated $L_\lambda^\uparrow$, $L_\lambda^\downarrow$, and τ_λ derived from MODTRAN with user supplied atmospheric parameters; we supplied matching parameters to the JPL standard product to facilitate comparison.

2.2.5. Water vapor scaling (WVS)

To apply WVS to the Delano scenes, we modified the base $L_\lambda^\uparrow$, $L_\lambda^\downarrow$, and τ_λ terms of Eq. (1) using Eqs. (5), (6), and (7) respectively:

$$L_\lambda'^{\uparrow}(\gamma) = L_\lambda^\uparrow(\gamma_1) * \frac{1-\tau_\lambda'(\gamma)}{1-\tau_\lambda(\gamma_1)} \tag{5}$$

$$L_\lambda'^{\downarrow}(\gamma) = a_\lambda + b_\lambda * L_\lambda'^{\uparrow}(\gamma) + c_\lambda * L_\lambda'^{\uparrow}(\gamma)^2 \tag{6}$$

$$\tau_\lambda'(\gamma) = \tau_\lambda(\gamma_1)^{\frac{\left(\gamma^{a_\lambda} - \gamma_2^{a_\lambda}\right)}{\left(\gamma_1^{a_\lambda} - \gamma_2^{a_\lambda}\right)}} * \tau_\lambda(\gamma_2)^{\frac{\left(\gamma_1^{a_\lambda} - \gamma^{a_\lambda}\right)}{\left(\gamma_1^{a_\lambda} - \gamma_2^{a_\lambda}\right)}} \tag{7}$$

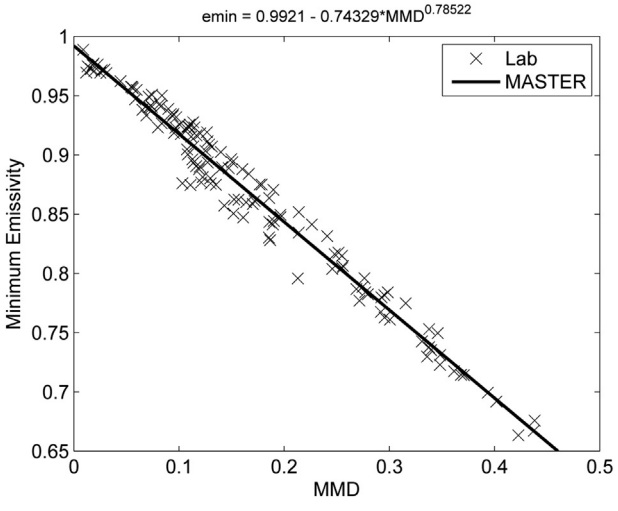

Fig. 3. MMD empirical regression for MASTER bands 43, 44, 47, 48, and 49.

where 'γ_1' and 'γ_2' are constants set to 0.7 and 1, and a, b, and c are the regression coefficients; an atmospheric term ($L_\lambda^\uparrow$, $L_\lambda^\downarrow$, or τ_λ) as a function of a subscripted γ_1 or γ_2 indicates the atmospheric term calculated using an amount of precipitable water vapor scaled by the corresponding constant. The band model parameter 'α_λ' and apparent surface brightness temperature 'T_{α_λ}' were determined using the Enhanced MultiChannel Water Vapor Dependent (EMC/WVD) split-window algorithm (Eqs. (8) and (9)) as described in Tonooka (2005) and Hulley and Hook (2011):

$$\alpha_\lambda = p_\lambda + q_\lambda W + r_\lambda W^2 \tag{8}$$

$$T_{a_\lambda} = \alpha_{\lambda,0} + \sum_{k=1}^{n} \alpha_{\lambda,k} T_k \tag{9}$$

where W is the precipitable water vapor in g/cm^2; n is the number of bands used in TES ($n = 5$); k is an assigned band number 1 through 5 for the corresponding band centered at wavelength λ; and p, q, and r are the regression coefficients as determined by a global simulation model using NCEP model data (Tonooka, 2001).

The WVS method takes per-band brightness temperatures at a given pixel calculated from Eq. (9), and an estimate of water vapor over that pixel to generate band-dependent scaling factors to modify and scale the $L_\lambda^\uparrow$, $L_\lambda^\downarrow$, and τ_λ terms of Eq. (1) to the $L_\lambda'\uparrow(\gamma)$, $L_\lambda'\downarrow(\gamma)$, and $\tau_\lambda'(\gamma)$ terms of Eqs. (5), (6), and (7). The per band and pixel WVS scaling factor 'γ' is calculated from the band model parameter 'α_λ' (Eq. (8)) and apparent surface brightness temperatures 'T_{α_λ}' using Eq. (10):

$$\gamma = \frac{\ln\left(\frac{\tau_\lambda(\gamma_2)^{\gamma_1{}^{\alpha_\lambda}}}{\tau_\lambda(\gamma_1)^{\gamma_2{}^{\alpha_\lambda}}} * \left(\frac{\frac{B_\lambda(T_{a_\lambda}) - L_\lambda^\uparrow(\gamma_1)}{1-\tau_\lambda(\gamma_1)}}{\frac{L_\lambda - L_\lambda^\uparrow(\gamma_1)}{1-\tau_\lambda(\gamma_1)}}\right)^{\gamma_1{}^{\alpha_\lambda} - \gamma_2{}^{\alpha_\lambda}}\right)}{\ln\left(\frac{\tau_\lambda(\gamma_2)}{\tau_\lambda(\gamma_1)}\right)}. \tag{10}$$

The 'γ' WVS scaling factors were only computed over graybody targets to minimize emissivity effects, and were then interpolated over any bare pixels on the scene using an inverse distance weighting interpolation. In contrast to the $L_\lambda^\uparrow$, $L_\lambda^\downarrow$, and τ_λ values retrieved from interpolated LUTs as described in Sections 2.2.4 and 2.2.3, and since the estimates of $L_\lambda^\uparrow$, $L_\lambda^\downarrow$, and τ_λ are scaled by water vapor separately, we used the same base $L_\lambda^\uparrow$, $L_\lambda^\downarrow$, and τ_λ estimates derived from MODTRAN run with NCEP inputs when deploying WVS.

These scaling factors were applied to both 1° water vapor estimates provided by NCEP, and also to the 13.1 m resolution water vapor maps that AVIRIS provided. Following the application of scaling factors using Eqs. (5) through (10), temperature and emissivity were retrieved using the TES method as described in the HyspIRI TES ATBD (Hulley, 2011).

2.3. Field data

Leaf water potential and gas exchange were measured on the flight day both at predawn and throughout the data acquisition flight windows, in six georeferenced vines per block (see Fig. 1) using a Scholander chamber (Soilmoisture 3005, Soilmoisture Equipment Corp., Santa Barbara, CA) and a LiCor 6400 (LiCor Inc., Lincoln, Nebraska, USA) respectively. The LiCor instrument calculates the temperature gradient between the ambient air and a sampled leaf as part of the gas exchange analysis routine, using a fine wire thermocouple installed in the chamber to measure and record leaf temperature while taking a simultaneous measurement of the ambient air temperature. Two instrumented towers, one per block, were installed at the site to estimate surface energy fluxes using the surface renewal technique (Castellv & Snyder, 2010; Paw U, Qiu, Su, Watanabe, & Brunet, 1995). These towers recorded a number of variables, including air temperature by fine wire thermocouple, at half hour intervals during the week preceding and following the data flight.

Averaged measurements of leaf temperature provide a close empirical measurement of directional vegetation kinetic temperature (hereafter referred to as *canopy temperature*), and also approximate the radiative temperature for the canopy that we expect at low zenith angles given that the leaves are large, the canopy is closed, and emissivity of leaves is known to be high (Norman, Chen, & Goel, 1990). Unfortunately, a mismatch of 1 to 1.5 h between the *in situ* LiCor measurements and the closest flight line prevented us from using these raw leaf temperature measurements as validation data. The hour offset between the end of the LiCor measurements and the data flight is present because stomatal conductance measurements were taken coincident with the data flight and it was not feasible to take LiCor measurements simultaneously; the half hour of additional temporal variability is due to the time required to traverse and sample both the North and South data blocks with the LiCor instrument. The differences in watering regimes between the North and South blocks introduce a spatial temperature gradient which is imposed on top of a diurnal temperature trend present over the half hour sampling window. In order to separate the temporal and spatial temperature trends present in the LiCor leaf temperature measurements, and ultimately adjust leaf temperatures measurements forward in time to match the acquisition time of the remote sensing data, we modeled an aspatial diurnal temperature trend using tower data measurements as described below.

2.3.1. Modeling diurnal temperature

To model the aspatial diurnal temperature trend, we used the following equation:

$$K(t) = A * \cos((W * t) + S) + M + (D * (t - 140)) \tag{11}$$

where A is the amplitude of the diurnal cycle (i.e., the range of the min/max temperature values); W is a shape parameter that corresponds to the width of the period; t is the time in decimal day of the year; S is an offset shift that determines the alignment and timing of the daily min/max temperature trough/peak; M is the mean daily temperature (centered on day 140); D is a linear term for the daily temperature trend; and $K(t)$ is the modeled temperature in kelvin at time t. We estimated the parameters for Eq. (11) using a non-linear-least-squares-function (NLLSF) (Nelder & Mead, 1965) fit to data from the North tower (Fig. 1). We selected tower data from three days (72-hours) prior and one day (24 h) after the data flight as input to the NLLSF fitting function; this range was chosen because it included four contiguous days about the data that shared similar atmospheric conditions—clear, low wind, and no clouds. The NLLSF function was also seeded with initial parameter guesses of the mean temperature, amplitude, and daily temperature trend by taking the mean of the dataset, the average difference between the min and max temperatures, and the best fit slope of the dataset respectively.

Since the North Tower was positioned at the edge of the vineyard, with an ambient air temperature sensor fixed 1 m above the vegetation canopy, the diurnal tower air temperature cycle was localized to a within canopy diurnal air temperature cycle using the LiCor measurements. The daily temperature trend D, and the timing of the daily minimum and maximum temperature as controlled by parameters S and W were assumed to be the same both within the canopy and at the North tower; the mean daily temperature M and daily temperature range A were known to not be the same from inspection of the LiCor predawn and afternoon measurements. Fixing D, S and W to the values calculated from the towers, we reran the NLLSF on the predawn and afternoon LiCor air temperature measurements to estimate values of M and A appropriate to within the vegetation canopy.

Please cite this article as: Grigsby, S.P., et al., Improved surface temperature estimates with MASTER/AVIRIS sensor fusion, *Remote Sensing of Environment* (2015), http://dx.doi.org/10.1016/j.rse.2015.05.019

3. Results

3.1. Remote sensing results

Results from the ACORN water vapor inversion using AVIRIS data are shown on the top of Fig. 4. While there is likely some elevated water vapor over crops due to active evapotranspiration compared to bare soils, this effect is probably exaggerated in the ACORN retrieval by albedo differences between surface types. Despite these albedo artifacts, the retrieved values are reasonable overall, and moving air masses are visible throughout the image over all surface types. These water vapor estimates were used as described in Section 2.2.5 to generate the per band 'γ' factor inputs for the WVS method, and the calculated 'γ' factor inputs provided by AVIRIS are shown in the bottom of Fig. 4 for a single example MASTER band (band 44). Comparing the WVS 'γ' scaling factors to water vapor shows similar spatial patterns, as expected. Values less than 1 in the water vapor scaling factors indicate that water vapor over the scene was overestimated by the NCEP data.

Water vapor estimates were used with each of the three retrieval methods discussed in Sections 2.2.3, 2.2.4, and 2.2.5; the result of the temperature retrievals is shown in Fig. 5. All three retrievals display similar spatial patterns, and show the North/South temperature gradient present from the different watering regimes applied to the different blocks. The temperature retrievals from TES and WVS that did not account for variable scene water vapor (*omitted*), showed similar spatial patterns, with some subtle spatial smoothing and loss of fine detail.

3.2. Validation data

Validation of our remote sensing data utilizes both measured and model results. While the measured leaf temperatures capture spatial variability, the temporal variability captured by model results is used to adjust leaf measurements to account for diurnal heating, as described in Section 2.3.1. The input data and result of the fit used to estimate the mean daily temperature trend (D), and shape parameters (W and S) can be seen in Fig. 6a. The amplitude (A) and mean temperature (M) parameters were localized within the canopy; the resulting parameter estimates of Eq. (11) for canopy temperature can be seen in Fig. 6b. The difference in slope between the model (blue line in Fig. 6b) and the within canopy air temperature observations is due to the strong North–South temperature gradient shown in Fig. 5 that matched the *in situ* sampling direction; thus, the parameters from Fig. 6b were used with Eq. (11) to estimate the aspatial (i.e., temporal) temperature trend within the canopy. While tower data measurements only include air temperature, and not leaf temperature, we found that the two temperature measurements were highly correlated throughout the sampling window and that air temperature can be used to predict leaf temperature using a simple linear regression:

$$leafTemp = 1.19 * AirTemp - 57.19. \quad (12)$$

We established this linear regression ($R^2 = 0.81$) using the air and leaf temperatures from the LiCor instrument; since each pair of measurements is collocated in both time and space, we believe the relationship is robust across the spatial and temporal gradients. Using this regression to estimate leaf (and canopy) temperatures at the time of the data flight explicitly assumed that the leaf temperature to air temperature relationship calculated using data collected from 1:30 pm to 2 pm was still valid at 3 pm. Since there is no major shift in the heating regime over this time as measured by the towers (*rnet*), and since the time offset is never more than 90 min, we believe this to be a sound assumption.

To capture the spatial variability in temperature within the data blocks shown in Fig. 5, we calculated residuals between the *in situ* measurements of air temperature recorded by the LiCor instrument, and the modeled air temperatures shown in Fig. 6b. These residuals were added back to the modeled air temperature at the time of the data flight to yield spatially explicit air temperature estimates at 3:01 pm PDT

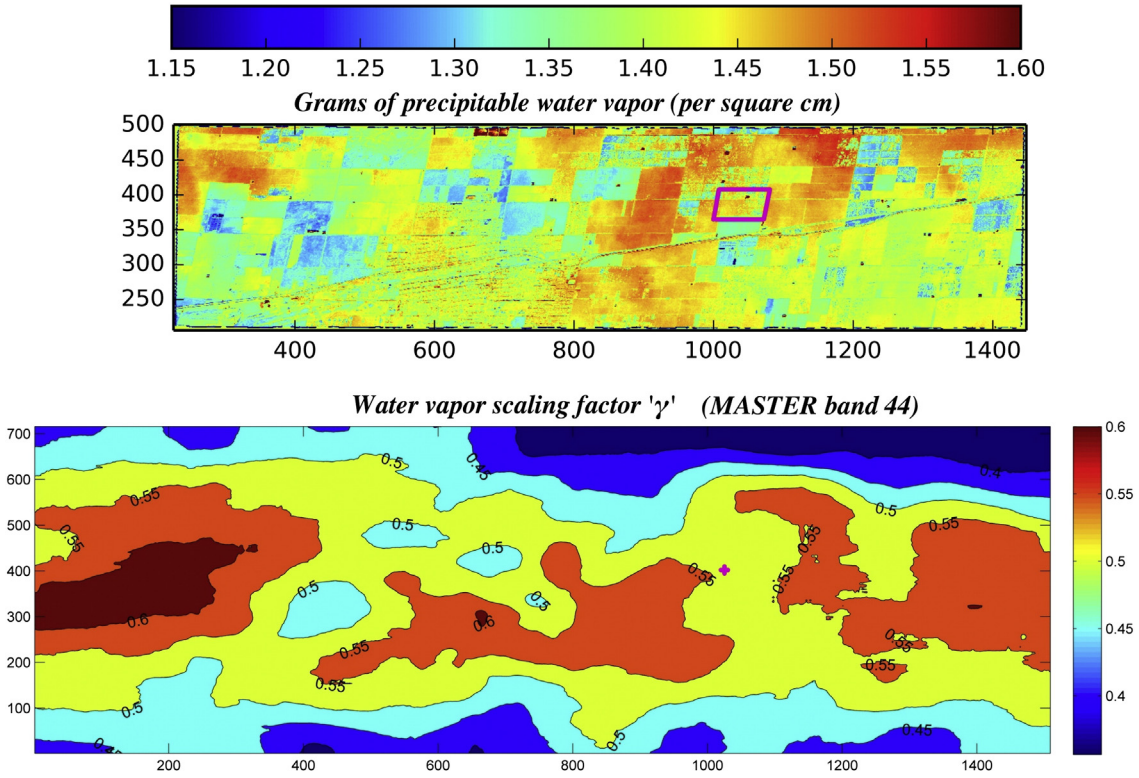

Fig. 4. (Top): AVIRIS derived water vapor; field site is denoted in purple box. (Bottom): WVS scaling factor for MASTER band 44 using AVIRIS derived water vapor estimate; purple '+' marks field validation site. The x-axis and y-axis coordinates are across track and along tract pixel coordinates for the MASTER sensor.

Please cite this article as: Grigsby, S.P., et al., Improved surface temperature estimates with MASTER/AVIRIS sensor fusion, *Remote Sensing of Environment* (2015), http://dx.doi.org/10.1016/j.rse.2015.05.019

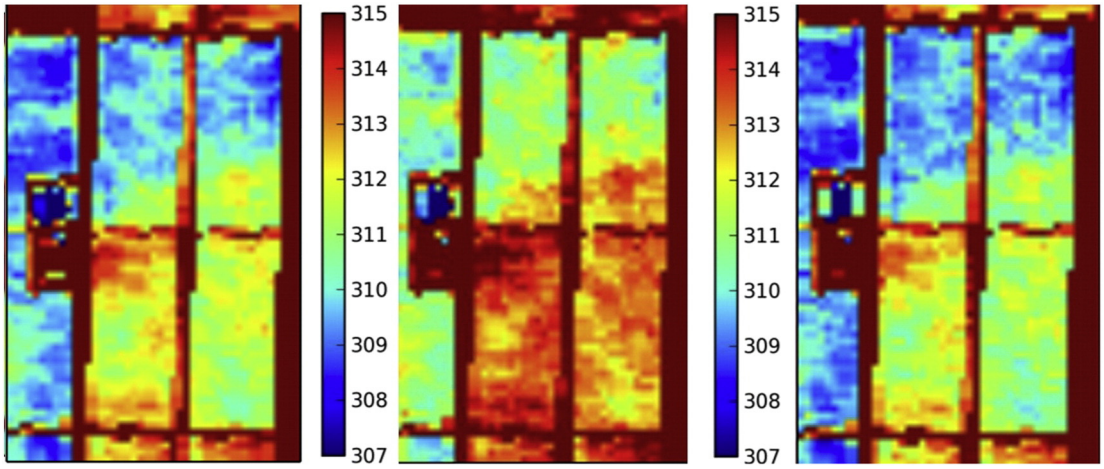

Fig. 5. Temperature retrievals at Delano Vineyards field site, units are kelvin. (Left): Constant emissivity (0.99). (Center): TES method. (Right): WVS + TES method. All panels use AVIRIS derived water vapor. The increasing trend of temperature from North-to-South is aligned with the North-to-South sampling order.

(22:01 UTC). The regression in Eq. (12) was used to convert air temperature within the canopy to leaf temperature; these adjusted measures of leaf temperature shown in Fig. 7 represent our best estimate of canopy temperature at the time of the data flights, and were used as independent verification data in assessing our remote sensing temperature retrievals.

3.3. TES evaluation

The accuracies of temperature retrievals from single-band inversion, TES, and WVS—with and without AVIRIS derived water vapor—are shown in Table 1 on the following page ( ). Although the TES + WVS method replaced TES as the new JPL temperature and emissivity standard product for all MASTER lines collected since 2013, we selected the older JPL TES product as our baseline in comparing temperature retrievals in Table 1 since the older TES method is available for all MASTER scenes. Our results show that there is a strong tendency for TES to overestimate surface canopy temperature as a consequence of underestimating emissivity. The addition of AVIRIS derived water vapor improved retrieval accuracy as expected, although still not to within a kelvin of estimated canopy temperature.

The WVS method showed significant improvement over TES, both with and without the addition of per pixel water vapor. For example, residuals between measured (Corrected LiCor) and modeled LST for the five approaches showed no significant bias for the Single Band, WVS + NCEP and WVS + AVIRISWV retrievals, with residuals distributed evenly above and below the reference temperature. By comparison, JPL standard TES with and without AVIRIS-WV had a negative bias in excess of 1 K (Table 1). Coarse scale NCEP water vapor data (1°) still yielded errors well under a kelvin RMSE and had over 70% reduction in error compared to the JPL product that WVS replaces. The addition of AVIRIS water vapor to the WVS method produced further improvements, reducing retrieval RMSE to less than 0.5 K.

4. Discussion

4.1. Spatial patterns

The dominant pattern of observed canopy temperature values in Fig. 5 shows the effects of different watering regimes in the North and South blocks. Additional fine scale spatial variability of temperature within the field is likely the result of water pressure drops in the irrigation line, differences in soil composition and water holding capacity, and/or other plant physiologic stresses such as pest infestation, disease or nutrient stress. The observed canopy temperature range at the vineyard—up to 8 K between the North and South blocks, and over 5 K within a single block—has substantial implications for productivity. Previous studies of woody vegetation have found that a difference of 7 to 8 K in canopy temperature corresponds to the difference between peak photosynthesis and photosynthesis at 75% of peak (Larcher,

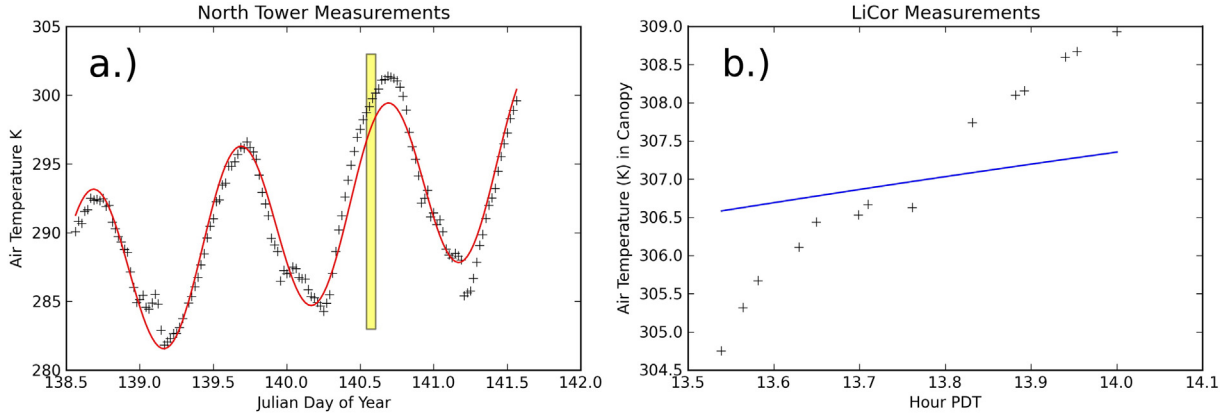

Fig. 6. (a.) Diurnal model (red line) fit to North Tower data (crosses); model parameters as fit by NLLSF ($\chi^2_{red} = 1.76$) are as follows: $A = 6.565$, $W = 6.264$, $S = -1.570$, $M = 290.736$, $D = 3.125$. Yellow box is the time window for *in situ* LiCor measurements. (b.) Diurnal aspatial temperature model (blue line) for canopy air temperature; model parameters $W = 6.264$, $S = -1.570$, and $D = 3.125$ are fixed and taken from panel a; model parameters $A = 9.62$, and $M = 297.605$ were determined by NLLSF fit to LiCor data. The modeled blue line represents the temporal trend only — LiCor data observations (crosses) encapsulate both a temporal trend and the spatial trend shown in Fig. 5.

Please cite this article as: Grigsby, S.P., et al., Improved surface temperature estimates with MASTER/AVIRIS sensor fusion, *Remote Sensing of Environment* (2015), http://dx.doi.org/10.1016/j.rse.2015.05.019

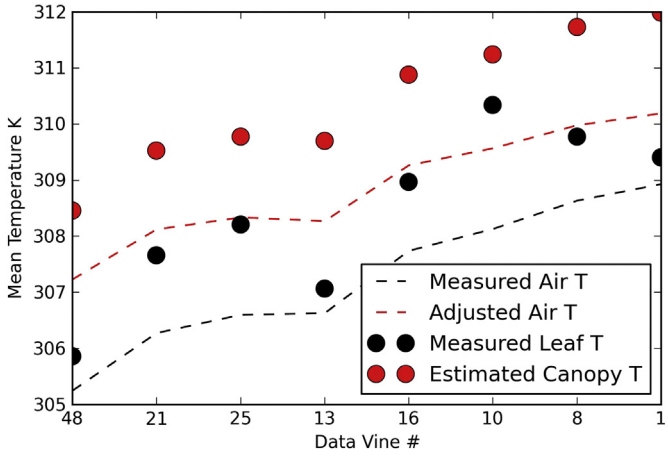

Fig. 7. Black symbols are observations 1 to 1.5 h prior to data flight. Red symbols are temperatures time adjusted to 15:01 PDT using Eq. (11) with the coefficients listed in Fig. 6b.

1969). Since plants reduce fruit production when stressed, the reduction of gross photosynthesis has an outsized impact on harvest yield; for the Delano field site there was a reduction in yield in terms of berry size and cluster size in the south block compared to the fully irrigated north block in the 2011 experiment.

4.2. Separation of atmospheric and ϵ_λ errors

Some insight into the major source of errors when applying the TES and WVS methods can be inferred from the high accuracy that the single band inversion method achieves. In cases where the prescribed ϵ_λ is close to the true emissivity, we can expect that the major source of error will be from the atmospheric $L_\lambda^\uparrow$, $L_\lambda^\downarrow$, and τ_λ terms. Since both the single band inversion and the TES retrieval using AVIRIS water vapor share identical per pixel values of $L_\lambda^\uparrow$, $L_\lambda^\downarrow$, and τ_λ—with the TES temperature retrieval decreasing in accuracy after calibrating emissivities—we can infer that the prescribed and constrained ϵ_λ values in the single band inversion are closer to the true ϵ_λ than the calibrated ϵ_λ values from TES. Furthermore, given the high overall accuracy of the single band inversion, for TES we can infer that relatively small atmospheric errors are propagating to much larger errors in emissivity (usually ϵ_λ underestimation). Hence, the higher temperature errors for TES relative to the single band inversion ultimately result from errors in the emissivity estimation, rather than atmospheric path radiance residuals in the Planck inversion. It is worth noting that in addition to outperforming TES in all cases, the single band inversion using AVIRIS water vapor also outperformed the WVS method without water vapor.

As discussed in Section 2.2.5, the WVS method scales the $L_\lambda^\uparrow$, $L_\lambda^\downarrow$, and τ_λ terms before applying the same TES technique to estimate ϵ_λ. Given the high accuracy of WVS without AVIRIS water vapor compared to both TES temperature retrievals, and the similar accuracy compared to the single band inversion, the primary mode of improvement for the WVS method appears to be a reduction of emissivity errors—even though this reduction is itself driven by the modification of $L_\lambda^\uparrow$, $L_\lambda^\downarrow$, and τ_λ terms ahead of emissivity estimation. While the WVS method without water vapor maps achieves a substantial reduction of error relative to TES, the addition of AVIRIS derived water vapor still yields an estimated 30% further reduction in relative temperature error.

4.3. Implications for the HyspIRI mission

We show improvements in temperature retrievals when synthesizing data from TIR and SWIR instruments, particularly using the WVS method proposed by JPL. Comparison of WVS applied with and without hyperspectral derived water vapor showed a statistically significant improvement in LST compared to standard TES. However, the study area was also small and further evaluation over a larger area and a greater range in environmental conditions is needed to evaluate its potential for HyspIRI.

Vegetated surfaces are typically challenging targets for emissivity inversion, and accurate temperature retrieval of these surfaces bodes well for our ability to invert less challenging surfaces such as soils, rocks and senesced plant material that have greater spectral contrast. Regardless of surface type, the degree of improvement in temperature retrieval with the WVS method is expected to scale, with greater improvements in areas more humid than the Central Valley. Given that the majority of water vapor occurs below the altitude of our flight lines, and the similarity of the MASTER instrument to the proposed HyspIRI instrument, it is reasonable to expect similar canopy temperature accuracy from HyspIRI over closed canopies in areas like the Central Valley, with increasing surface temperature retrieval accuracy for heterogenous non-graybody pixels such as bare soil or exposed rock.

While the synthesis of hyperspectral derived water vapor and TIR data will only be possible for the 150 km swath of the HyspIRI VSWIR instrument (as opposed to the 600 km TIR radiometer swath), the technique remains a potentially powerful option to use over more complex terrain with a higher degree of spatial variability in column water vapor. Flights with AVIRIS that simulate the swath width and pixel size of the HyspIRI mission (and traverse both the Central Valley and the Sierra Nevadas) show both regional air masses and significant terrain-related variation in column water vapor that follows path length and is inversely correlated with elevation (Thompson et al., in press, also this issue). Since total precipitable water vapor is strongly correlated with elevation, the relative improvements that we observed when

Table 1
Comparison of temperature retrievals from remote sensing data with field validation data. RMSE values are calculated relative to corrected LiCor field measurements, and are weighted according to the number of observations occurring within the corresponding pixel. The JPL standard TES product is representative of the 1999–2013 operational retrievals performed by NASA for ASTER, MODIS, and MASTER instruments, and is used as our baseline when comparing percent error reduction between temperature retrieval methods.

	Corrected LiCor		Single-band inversion		Temperature–emissivity separation				Water vapor scaling			
	Leaf temperature		*AVIRISWV*		*JPL standard*		*AVIRISWV*		*NCEP*		*AVIRISWV*	
Vine	*N Obs*	*meantemp*	*temp*	*resids*	*temp*	*resids*	*temp*	*resids*	*temp*	*resids*	*temp*	*resids*
48	3	308.46	309.06	−0.60	311.70	−3.24	310.14	−1.68	309.60	−1.14	308.97	−0.51
21	2	309.52	309.25	0.27	311.19	−1.67	310.25	−0.73	309.76	−0.24	309.59	−0.07
25	2	309.78	309.81	−0.03	311.34	−1.56	310.83	−1.05	309.49	0.29	309.33	0.45
13	1	309.70	309.26	0.44	310.90	−1.20	310.61	−0.91	309.51	0.19	309.29	0.41
16	1	310.88	312.45	−1.57	314.07	−3.19	314.05	−3.17	312.35	−1.47	312.28	−1.40
10	2	311.24	312.15	−0.91	314.10	−2.86	313.06	−1.82	311.65	−0.41	311.40	−0.16
8	2	311.73	312.19	−0.46	313.87	−2.14	313.44	−1.71	311.92	−0.19	311.80	−0.07
1	1	311.98	312.24	−0.26	313.52	−1.54	313.46	−1.48	312.03	−0.05	311.91	0.07
N Obs weighted RMSE (K)			0.66		2.41		1.63		0.70		0.49	
% error reduction			72.8%		–		32.3%		71.1%		79.6%	

Please cite this article as: Grigsby, S.P., et al., Improved surface temperature estimates with MASTER/AVIRIS sensor fusion, *Remote Sensing of Environment* (2015), http://dx.doi.org/10.1016/j.rse.2015.05.019

using AVIRIS derived water vapor in place of NCEP provided water vapor are likely conservative for what we can expect in areas of greater topographic variability than the Central Valley. In other words, although we do not yet know the absolute temperature retrieval accuracy for all atmospheric conditions or over complex terrain, a flat homogenous area—such as our study site—under utilizes the potential benefit and improvement of using spatially explicit water vapor. Thus, at the regional scale, we would anticipate WVS with AVIRIS-derived water vapor to be even more significant.

The improved temperature retrievals that we demonstrate using WVS over graybody pixels are dominated by a reduction in propagated error in estimating surface emissivity—a result that portends a future for the HyspIRI mission focused on other, non-atmospheric challenges. Chief among these challenges will likely be the scaling issues inherent in estimating canopy scale physical phenomena using a 60 meter HyspIRI pixel. Orchard cash crops such as almonds and pistachios present a multisource emission target, as do pixels that cover multiple adjacent plots—and all of which will require multimember definitions of surface temperature to be meaningful. Ultimately, further refinement of temperature estimates will require modeling endmember fractions and thermal unmixing of the surface cover that accounts for varying endmember emissivity and temperature within a pixel. The HyspIRI mission will be well equipped to accomplish the former using established mixture analysis methods in the VSWIR, however the latter will necessitate dealing with substantial nonlinearities present in TIR mixing.

One potential approach for future studies that aim to tackle this unmixing challenge is to modify the split-window approach. The split-window approach pioneered by Dozier (1981) solves for endmember fractions and temperature simultaneously, given known endmember emissivities. Since hyperspectral measurements can provide accurate fractional cover estimates, direct inversion of emissivity from WVS corrected radiant emission and endmember fractions may be possible within an error minimization framework that uses total at sensor radiance as way to constrain the solution space.

5. Conclusion

Results of this study highlight our ability to correct for atmospheric water vapor errors in the use of TIR to retrieve canopy temperature. Plant canopy temperature is a plant physiological state variable that controls gross photosynthesis by limiting or enhancing carbon uptake, transpiration, and respiration. Retrieving canopy temperature at subkelvin accuracy will allow farmers and scientists to assess when vegetation respiration is increasing faster than photosynthesis, quantify the total hydrologic exchange with the atmosphere, and pinpoint heat stress that directly reduces photosynthesis rates due to enzyme inactivation. At the field scale, accurate canopy temperature measurements are crucial to efficient water use in agriculture where transpiration rates are used to assess water loss to the atmosphere; at regional spatial scales, canopy temperature maps heat damage and forecasts yield reduction or failure in crops, and also provides insight into the respiration rates of heterogenous natural biomes. Modeling vegetation as multisource emission targets of varying temperatures will likely yield further improvements in canopy temperature estimation, especially for heterogenous ecosystems or crops such as orchards that do not present a uniform closed canopy.

Acknowledgments

The research described in this paper was initiated with support by the NASA Student Airborne Research Program (SARP) through the University of North Dakota as part of the NASA Ames Cooperative for Research in Earth Science and Technology (ARC-CREST) Award Number NNX12AD05A, Sub-award NNX12AD05A-UND1, and was carried out at the University of California Santa Barbara. We gratefully thank both Rose Dominguez and Jeff Myers at UARC for their assistance with MASTER calibration data, as well as Dr. David R. Smart and the USDA Specialty Crops Research Initiative (SCRI) headed by Dr. Patrick Brown (PI) for their role in collecting the ground measurements at Delano Vineyards. In addition, we thank the two anonymous reviewers for their helpful comments, which were instrumental in adding additional clarity to many parts of this text.

References

Allen, R. G., Pereira, L. S., Raes, D., & Smith, M. (1998). *Crop evapotranspiration: Guidelines for computing crop requirements. Irrigation and Drainage Paper No. 56*, Rome, Italy: FAO.

Alsina, M.M., Cheng, T., Riaño, D., Whiting, M., Ustin, S., & Smart, D.R. (2013). Water status detection in California table grapes: from leaf to airborne. *Precision agriculture, 13*. (pp. 225–231). Springer.

Anderson, M.C., Norman, J.M., Kustas, W.P., Houborg, R., Starks, P.J., & Agam, N. (2008). A thermal-based remote sensing technique for routine mapping of land-surface carbon, water and energy fluxes from field to regional scales. *Remote Sensing of Environment, 1120*, 4227–4241.

Baldridge, A.M., Hook, S.J., Grove, C.I., & Rivera, G. (2009). The ASTER spectral library version 2.0. *Remote Sensing of Environment, 1130*(4), 711–715.

Berk, Alexander, Anderson, Gail P., Acharya, Prabhat K., Bernstein, Lawrence S., Muratov, Leon, Lee, Jamine, et al. (2005). MODTRAN 5: a reformulated atmospheric band model with auxiliary species and practical multiple scattering options: update. *Defense and Security* (pp. 662–667). International Society for Optics and Photonics.

Berk, A., Bernstein, L.S., Anderson, G.P., Acharya, P.K., Robertson, D.C., Chetwynd, J.H., et al. (1998). MODTRAN cloud and multiple scattering upgrades with application to AVIRIS. *Remote Sensing of Environment, 650*(3), 367–375.

Berk, Alexander, Bernstein, Lawrence S., & Robertson, David C. (1987). MODTRAN: a moderate resolution model for LOWTRAN. *Technical report, DTIC document*.

Carrère, Veronique, & Conel, James E. (1993, May). Recovery of atmospheric water vapor total column abundance from imaging spectrometer data around 940 nm — sensitivity analysis and application to Airborne Visible/Infrared Imaging Spectrometer (AVIRIS) data. *Remote Sensing of Environment, 440*(2–3), 179–204. http://dx.doi.org/10.1016/0034-4257(93)90015-p (ISSN 0034–4257).

Castellv, F., & Snyder, R.L. (2010). A new procedure based on surface renewal analysis to estimate sensible heat flux: a case study over grapevines. *Journal of Hydrometeorology, 110*(2), 496–508.

CDFA (2013). Agricultural statistical review. *Technical report*. Sacramento CA: California Department of Food and Agriculture.

Cheng, Tao, Riaño, David, Koltunov, Alexander, Whiting, Michael L., Ustin, Susan L., & Rodriguez, Jenna (2013). Detection of diurnal variation in orchard canopy water content using MODIS/ASTER airborne simulator (master) data. *Remote Sensing of Environment, 132*, 1–12.

Cheng, Tao, Riaño, David, & Ustin, Susan L. (2014). Detecting diurnal and seasonal variation in canopy water content of nut tree orchards from airborne imaging spectroscopy data using continuous wavelet analysis. *Remote Sensing of Environment, 143*, 39–53.

Courault, Dominique, Seguin, Bernard, & Olioso, Albert (2005, Nov). Review on estimation of evapotranspiration from remote sensing data: from empirical to numerical modeling approaches. *Irrigation and Drainage Systems, 190*(3–4), 223–249. http://dx.doi.org/10.1007/s10795-005-5186-0 (ISSN 1573–0654).

Dozier, Jeff (1981). A method for satellite identification of surface temperature fields of subpixel resolution. *Remote Sensing of Environment, 11*, 221–229.

Escalona, José Mariano, Flexas, Jaume, & Medrano, H. (2000). Stomatal and non-stomatal limitations of photosynthesis under water stress in field-grown grapevines. *Functional Plant Biology, 270*(1), 87-87. http://dx.doi.org/10.1071/PP99019_CO.

Flexas, Jaume, Bota, Josefina, Cifre, Josep, Mariano Escalona, José, Galmés, Jeroni, Gulas, Javier, et al. (2004). Understanding down-regulation of photosynthesis under water stress: future prospects and searching for physiological tools for irrigation management. *Annals of Applied Biology, 1440*(3), 273–283.

Gao, Bo-Cai, & Goetz, Alexander F.H. (1990). Column atmospheric water vapor and vegetation liquid water retrievals from Airborne Imaging Spectrometer data. *Journal of Geophysical Research, 950*(D4), 3549. http://dx.doi.org/10.1029/jd095id04p03549 (ISSN 0148–0227).

Gillespie, A., Rokugawa, S., Matsunaga, T., Cothern, J.S., Hook, S., & Kahle, A.B. (1998, Jul). A temperature and emissivity separation algorithm for Advanced Spaceborne Thermal Emission and Reflection Radiometer (ASTER) images. *IEEE Transactions on Geoscience and Remote Sensing, 360*(4), 1113–1126. http://dx.doi.org/10.1109/36.700995 (ISSN 0196–2892).

Girona, J., Mata, M., Del Campo, J., Arbonés, A., Bartra, E., & Marsal, J. (2006). The use of midday leaf water potential for scheduling deficit irrigation in vineyards. *Irrigation Science, 240*(2), 115–127.

Green, R. O., Conel, J. E., Margolis, J. S., Bruegge, C. J., & Hoover, G. L. (1991). An inversion algorithm for retrieval of atmospheric and leaf water absorption from AVIRIS radiance with compensation for atmospheric scattering. *Annual JPL Airborne Visible/Infrared Imaging Spectrometer (AVIRIS) Workshop, Volume 3*, 51–61 JPL Publication 91-28.

Green, Robert O., Conel, James E., & Roberts, Dar A. (1993, Sep). Estimation of aerosol optical depth, pressure elevation, water vapor, and calculation of apparent surface reflectance from radiance measured by the airborne visible/infrared imaging spectrometer (AVIRIS) using a radiative transfer code. *Imaging Spectrometry of the Terrestrial Environment*. http://dx.doi.org/10.1117/12.157054.

Please cite this article as: Grigsby, S.P., et al., Improved surface temperature estimates with MASTER/AVIRIS sensor fusion, *Remote Sensing of Environment* (2015), http://dx.doi.org/10.1016/j.rse.2015.05.019

Gustafson, William T., Gillespie, Alan R., & Yamada, Gail J. (2006). Revisions to the ASTER temperature/emissivity separation algorithm. *2nd International Symposium on Recent Advances in Quantitative Remote Sensing*.

Hook, Simon J., Myers, Jeffrey J., Thome, Kurtis J., Fitzgerald, Michael, & Kahle, Anne B. (2001, Apr). The MODIS/ASTER airborne simulator (MASTER) — a new instrument for earth science studies. *Remote Sensing of Environment*, *760*(1), 93–102. http://dx.doi.org/10.1016/s0034-4257(00)00195-4 (ISSN 0034–4257).

Howitt, Richard, Medellin-Azuara, Josue, & Lund, Jay (2014). *Preliminary 2014 Drought Economic Impact Estimates in Central Valley Agriculture.*

Hsiao, Theodore C. (1973). Plant responses to water stress. *Annual Review of Plant Physiology*, *240*(1), 519–570.

Hulley, Glenn C. (2011). *HyspIRI Level-2 Thermal Infrared (TIR) land surface temperature and emissivity algorithm theoretical basis document.* Pasadena, CA: Jet Propulsion Laboratory, National Aeronautics and Space Administration.

Hulley, Glynn C., & Hook, Simon J. (2009). The North American ASTER land surface emissivity database (NAALSED) version 2.0. *Remote Sensing of Environment*, *1130*(9), 1967–1975.

Hulley, G., & Hook, S. (2011). *HyspIRI Level-2 TIR surface radiance algorithm theoretical basis document.*

Hulley, Glynn C., Hughes, Christopher G., & Hook, Simon J. (2012). Quantifying uncertainties in land surface temperature and emissivity retrievals from ASTER and MODIS thermal infrared data. *Journal of Geophysical Research*, *1170*(D23). http://dx.doi.org/10.1029/2012jd018506.

Hulley, Glynn, Veraverbeke, Sander, & Hook, Simon (2014). Thermal-based techniques for land cover change detection using a new dynamic MODIS multispectral emissivity product (MOD21). *Remote Sensing of Environment*, *140*, 755–765.

Jackson, Ray D., Idso, S.B., Reginato, R.J., & Pinter, P.J. (1981). Canopy temperature as a crop water stress indicator. *Water Resources Research*, *170*(4), 1133–1138.

Jarvis, P.G., & McNaughton, K.G. (1986). Stomatal control of transpiration: scaling up from leaf to region. *Advances in Ecological Research*, 1–49. http://dx.doi.org/10.1016/s0065-2504(08)60119-1 (ISSN 0065–2504).

Kliewer, W.M., Freeman, & Hossom, C. (1983). Effect of irrigation, crop level and potassium fertilization on Carignan vines. I. Degree of water stress and effect on growth and yield. *American Journal of Enology and Viticulture*, *34*, 186–196.

Larcher, W. (1969). *Effect of environmental and physiological variables on the carbon dioxide gas exchange of trees.* Photosynthetica.

Matsunaga, T. (1994). A temperature-emissivity separation method using an empirical relationship between the mean, the maximum, and the minimum of the thermal infrared emissivity spectrum. *Journal of the Remote Sensing Society of Japan*, *140*(2), 230–241.

Matthews, Mark A., & Anderson, Michael M. (1989). Reproductive development in grape (*Vitis vinifera* L.): responses to seasonal water deficits. *American Journal of Enology and Viticulture*, *400*(1), 52–60.

McCutchan, Harold, & Shackel, K.A. (1992). Stem-water potential as a sensitive indicator of water stress in prune trees (*Prunus domestica* L. cv. French). *Journal of the American Society for Horticultural Science*, *1170*(4), 607–611.

Monteith, J.L., et al. (1965). Evaporation and environment. *Symp. Soc. Exp. Biol*, *Volume 19*. (pp. 4).

Nelder, J.A., & Mead, R. (1965, Jan). A simplex method for function minimization. *The Computer Journal*, *70*(4), 1460–2067. http://dx.doi.org/10.1093/comjnl/7.4.308.

Norman, John M., Chen, Jia-lin, & Goel, Narendra (1990). Thermal emissivity and infrared temperature dependence on plant canopy architecture and view angle. *Geoscience and Remote Sensing Symposium, 1990. IGARSS '90. 'Remote Sensing Science for the Nineties'., 10th Annual International* (pp. 1747–1750). IEEE.

Paw U, Kyaw Tha, Qiu, Jie, Su, Hong-Bing, Watanabe, Tomonori, & Brunet, Yves (1995). Surface renewal analysis: a new method to obtain scalar fluxes. *Agricultural and Forest Meteorology*, *740*(1–2), 119–137. http://dx.doi.org/10.1016/0168-1923(94)02182-J (ISSN 0168–1923, URL http://www.sciencedirect.com/science/article/pii/016819239402182J).

Realmuto, V. J. (1990). Separating the effects of temperature and emissivity: emissivity spectrum normalization. *Proc. 2nd TIMS Workshop*, 55–90 JPL Publication.

Roberts, Dar A., Quattrochi, Dale A., Hulley, Glynn C., Hook, Simon J., & Green, Robert O. (2012, Feb). Synergies between VSWIR and TIR data for the urban environment: an evaluation of the potential for the Hyperspectral Infrared Imager (HysplRI) Decadal Survey mission. *Remote Sensing of Environment*, *117*, 83–101. http://dx.doi.org/10.1016/j.rse.2011.07.021 (ISSN 0034–4257).

Scheele, C.J., Rill, L., Grigsby, S., & Ustin, S. (2013). Land surface temperature retrieval through the synthesis of hyperspectral and multispectral data from the HyspIRI preparatory flight campaign. *AGU Fall Meeting Abstracts*, *Volume 1*. (pp. 0457).

Schultz, Hans R., & Matthews, Mark A. (1988). Vegetative growth distribution during water deficits in *Vitis vinifera* L. *Functional Plant Biology*, *150*(5), 641–656.

Shackel, Kenneth A., Ahmadi, H., Biasi, W., Buchner, R., Goldhamer, D., Gurusinghe, S., et al. (1997). Plant water status as an index of irrigation need in deciduous fruit trees. *HortTechnology*, *70*(1), 23–29.

Thompson, David R., Gao, Bo-Cai, Green, Robert O., Roberts, Dar A., Dennison, Philip E., & Lundeen, Sarah R. (2015). Atmospheric correction for global mapping spectroscopy: ATREM advances for the HyspIRI preparatory campaign. *Remote Sensing of Environment* (in press, also this issue).

Tonooka, Hideyuki (2001). An atmospheric correction algorithm for thermal infrared multispectral data over land—a water-vapor scaling method. *IEEE Transactions on Geoscience and Remote Sensing*, *390*(3), 682–692.

Tonooka, Hideyuki (2005). Accurate atmospheric correction of ASTER thermal infrared imagery using the WVS method. *IEEE Transactions on Geoscience and Remote Sensing*, *430*(12), 2778–2792.

Zhengming, Wan, & Dozier, J. (1989, May). Land-surface temperature measurement from space: physical principles and inverse modeling. *IEEE Transactions on Geoscience and Remote Sensing*, *270*(3), 268–278. http://dx.doi.org/10.1109/36.17668 (ISSN 0196–2892).

Please cite this article as: Grigsby, S.P., et al., Improved surface temperature estimates with MASTER/AVIRIS sensor fusion, *Remote Sensing of Environment* (2015), http://dx.doi.org/10.1016/j.rse.2015.05.019